On the behaviour of the upstream-travelling waves in merging twin-jet systems

Michael Stavropoulos, Eduardo Martini, Daniel Edgington-Mitchell, Joel Weightman, Peter Jordan, Petrônio A.S. Nogueira

On the behaviour of the guided jet mode in merging twin-jet systems

Michael N. Stavropoulos[1]†, Eduardo Martini[2], Daniel M. Edgington-Mitchell[1], Joel Weightman[1], Peter Jordan[2], and Petrônio A. S. Nogueira[1]

[1]Department of Mechanical and Aerospace Engineering, Laboratory for Turbulence Research in Aerospace and Combustion, Monash University, Clayton 3800, Australia

[2]Département Fluides, Thermique, Combustion, Institut Pprime, CNRS-Université de Poitiers-ENSMA, Poitiers, France

(Received xx; revised xx; accepted xx)

There is currently considerable interest in the guided jet mode, as a result of recent works demonstrating it being the upstream component closing the loop of various resonant systems. For given supersonic jet operating conditions the mode is known to exist over only a finite-frequency range that, for a twin-jet system, has been observed to vary with both jet separation and solution symmetry. Vortex-sheet and finite-thickness linear stability models are employed to consider the behaviour of the guided jet mode as the two jets are brought together for both a planar and round twin-jet system. It is demonstrated that in both cases as the twin-jet system merges it forms a higher-order mode of an equivalent single-jet geometry. This then imposes a constraint on the guided jet mode as the existence region must change to meet the existence region of the equivalent geometry the system merges to, leading to the previously observed dependence on jet separation.

Key words: Authors should not enter keywords on the manuscript

1. Introduction

Modelling of coherent structures in jet flow has been of interest since pioneering works by Mollo-Christensen (1967) and Crow & Champagne (1971) demonstrated their presence in the previously considered stochastic flow. Among the structures considered is the upstream-propagating guided jet mode (k_p^-), a mode first studied by Tam & Hu (1989). It is characterised as having a phase speed very close to the speed of sound, maintaining radial structure outside of the jet core (as such not confined within it) and travelling upstream towards the nozzle (Tam & Hu 1989). For a supersonic jet, at any given set of jet-operating conditions this mode will be propogative only within a finite band of frequencies - referred to as the existence region of the mode. The lower bound of this frequency band, where the mode moves away from the sonic line describing the free-stream sound waves, is referred to as the branch point (cut-on) and the upper bound as the saddle point (cut-off). This saddle point is formed between the k_p^- mode and a downstream-propagating duct-like mode (k^+) (Towne *et al.* 2017). For frequencies above the saddle point the k_p^- mode becomes evanescent, whereas it is convectively neutral between the branch and saddle points.

† Email address for correspondence: michael.stavropoulos@monash.edu

Recent interest in the k_p^- mode has been motivated through the study of aeroacoustic resonance. The feedback loop characterising a given form of resonance consists of four components (Edgington-Mitchell 2019). The first is a downstream-propagating disturbance, often taken to be the Kelvin-Helmholtz (KH) mode, to some point downstream of the nozzle. Second is an interaction converting it to an upstream-propagating disturbance, being the third component of resonance. This disturbance then travels back to the nozzle where, via another interaction, it then excites a new downstream-propagating disturbance, the last component, and so closes the resonance loop. The form of the upstream-propagating component was historically considered to be a free-stream acoustic wave (Powell 1953), however recent work has suggested that it is instead the k_p^- mode which acts as the upstream component to close the resonance loop. A range of cases that have considered the k_p^- mode to close resonance include; an impinging jet (Tam & Ahuja 1990), jet-edge interaction (Jordan *et al.* 2018), and screech for both single (Shen & Tam 2002; Gojon *et al.* 2018; Edgington-Mitchell *et al.* 2018; Mancinelli *et al.* 2021) and twin (Nogueira & Edgington-Mitchell 2021; Stavropoulos *et al.* 2022) round jets. For the case of screech, high-amplitude discrete-frequency acoustic tones present in non-ideally expanded jets (Raman 1999; Edgington-Mitchell 2019), the finite existence region of the k_p^- mode then also serves as part of an explanation for the cut-on and cut-off of the screech tones (Mancinelli *et al.* 2019; Stavropoulos *et al.* 2023). Recent work by Edgington-Mitchell *et al.* (2021), following the hypothesis put forth by Tam & Tanna (1982), has demonstrated how interactions between the KH mode and the shock-cell structure can result in the creation of new waves, including the k_p^- mode. Later in Nogueira *et al.* (2022) it was shown that the KH interacts with both the primary and sub-optimal shock-cell wavenumbers to give rise to the k_p^- mode for different screech tones. As the shock-cell structure exhibits variations in the axial direction (Harper-Bourne & Fisher 1974), sub-optimal wavenumbers appear when taking an axial Fourier transform and thus represent these variations. This was then generalised by Edgington-Mitchell *et al.* (2022) to explain the observed screech mode staging (Merle 1957; Powell *et al.* 1992) in a round single jet.

The introduction of a second jet introduces additional complexities to the flow, as indicated through measurements of inter-jet pressure exceeding twice that of the single-jet value (Seiner *et al.* 1988), along with the complex, and often intermittent, coupling behaviour observed (Raman *et al.* 2012; Bell *et al.* 2021; Wong *et al.* 2023). Two new parameters introduced by the addition of a second jet are the jet separation distance and the symmetry of the system about each plane. Prior applications of linear stability theory to the round twin-jet system have shown how these parameters affect the growth rate of the KH mode (Morris 1990) and the allowable coupling forms (Rodríguez *et al.* 2022). For the k_p^- mode (upstream component in resonance) these parameters also play a role as they have been seen to affect its existence region (Du 1993; Stavropoulos *et al.* 2023). However, there is not currently an explanation as to why this behaviour occurs for the k_p^- mode.

In this work linear stability models will be applied to the supersonic twin-jet case, for both planar and round geometries, to examine the behaviour of the k_p^- mode as a function of the added twin-jet parameters jet separation and symmetry. Through considering changes in frequency of the k_p^- mode branch and saddle points, and thus the existence region of the mode, along with their radial structure, an explanation for why these characteristics are dependent on jet separation and symmetry will be sought.

The paper is organised as follows. The formulations for the numerical models, vortex-sheet and finite-thickness, utilised are outlined in §2. Results are shown in §3, with concluding remarks made in §4.

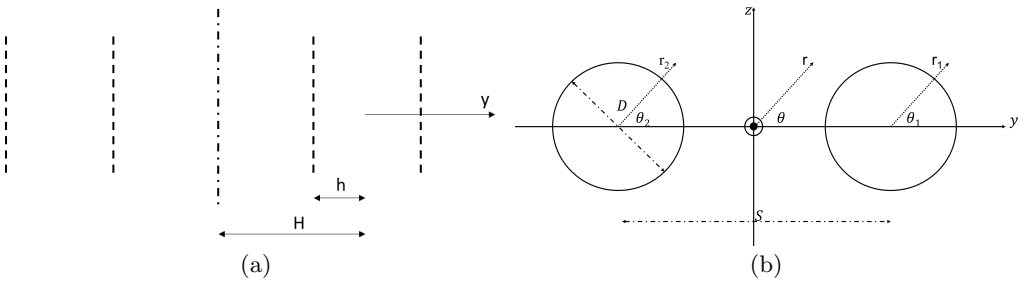

Figure 1: Setup of both the planar (a), and round (b) twin-jet geometries.

2. Mathematical models

2.1. *Planar twin-jet vortex-sheet model*

The planar twin-jet vortex-sheet model considered herein builds upon the planar single-jet model detailed in Martini *et al.* (2019). The planar jet is formed using two vortex sheets, each representing an infinitesimal-width shear layer across which both pressure and displacement are constant (Lessen *et al.* 1965; Michalke 1970; Morris 2010). To extend this to a planar twin-jet configuration, the symmetry line previously imposed at $y = 0$ for the single-jet case, is moved to a position of $y = -H$, the midpoint of the twin-jet system, and no assumptions are made about the symmetry of the flow within each individual jet. This resultant configuration is illustrated in figure 1a. The two jets are separated by a total distance $2H$ and the length-scale used for non-dimensionalisation is the jet half-width h. Perturbations about the system of the form

$$\tilde{P} = P(y)e^{i(kx-\omega t)}, \tag{2.1}$$

are considered where k is the wavenumber and ω frequency. Following Martini *et al.* (2019) the form of the perturbed pressure amplitude $P(y)$, referred to as the pressure eigenfunction, which in a given region takes the form

$$P(y) = C_a e^{\lambda_{i,o} y} + C_b e^{-\lambda_{i,o} y}. \tag{2.2}$$

The constants C_a and C_b in 2.2 are referred to as eigenfunction coefficients, and $\lambda_{i,o}$ is

$$\lambda_i = \sqrt{k^2 - \frac{1}{T}(\omega - Mk)^2},$$
$$\lambda_0 = \sqrt{k^2 - \omega^2}, \tag{2.3}$$

where M is the acoustic Mach number, and T the temperature ratio between jet and free-stream. Boundary conditions imposed on the twin-jet system are, continuity of pressure and displacement across each vortex sheet, bounding of the solution as $y \to \infty$, and imposing the symmetry condition at the midpoint of the two jets ($y = -H$). This symmetry condition is the solution having either zero gradient (symmetric) or is zero-valued (anti-symmetric). This results in the matrix equation

$$\boldsymbol{A}(k)\boldsymbol{c} = \boldsymbol{0}, \tag{2.4}$$

where $\boldsymbol{c}$ contains the eigenfunction coefficients. Further details on the matrix terms can be found in Appendix B. Setting the determinant of $\boldsymbol{A}$ equal to zero forms the dispersion relation for the planar twin jet and is used to obtain k, the system eigenvalue, for a given

set of jet parameters. Once a given k has been found, 2.4 can then be used to obtain the corresponding eigenfunction coefficients $\boldsymbol{c}$.

For considerations of the single planar jet the dispersion relation given in Martini *et al.* (2019) is used,

$$tanh(\lambda_i)^{\pm 1} + \frac{1}{T}(1 - \frac{kM}{\omega})^2(\frac{\lambda_o}{\lambda_i}) = 0, \tag{2.5}$$

with the pressure eigenfunctions given by,

$$P(y) = \begin{cases} \dfrac{e^{\lambda_i} \pm e^{-\lambda_i}}{e^{-\lambda_o}} e^{-\lambda_o y}, & y \geqslant h \\ e^{\lambda_i y} \pm e^{-\lambda_i y}, & -h \leqslant y \geqslant h \\ \dfrac{e^{-\lambda_i} \pm e^{\lambda_i}}{e^{-\lambda_o}} e^{\lambda_o y}, & y \leqslant -h \end{cases} \tag{2.6}$$

where the $\pm$ terms in 2.5 and 2.6 indicate the symmetric or anti-symmetric solution, about the jet centre, respectively. A further generalisation of the planar vortex-sheet model for a system of N jets is provided in Appendix D.

2.2. *Finite-thickness model*

The finite-thickness model follows the formulation used previously for round twin-jet systems (Nogueira & Edgington-Mitchell 2021; Stavropoulos *et al.* 2023). The two jets, each of diameter D, are separated by a centre-to-centre distance S as illustrated in figure 1(b). Solutions for the twin-jet system are denoted as either, SS, SA, AS, or AA, where each letter denotes symmetry (S) or anti-symmetry(A) about the $x-y$ and $x-z$ planes respectively (Rodríguez *et al.* 2018). All parameters are non-dimensionalised by D, free-stream sound speed, and density. The generalised eigenvalue problem can be expressed, here in terms of pressure, in the form

$$\mathbf{L}\hat{P} = k\mathbf{R}\hat{P}, \tag{2.7}$$

with $\hat{P} = Pe^{i\mu\theta}$ and operators $\mathbf{L}$ and $\mathbf{R}$ functions of the mean flow, its derivatives, and flow variables ω, M_j, S, and the ratio of specific heats γ. Here μ is the Floquet exponent resulting from the Floquet ansatz which is associated with the different symmetries of the flow (Nogueira & Edgington-Mitchell 2021), $\mu = 0$ describes a solution that is symmetric about the $x-z$ plane and $\mu = 1$ is anti-symmetric about it. Equation 2.7 utilises a Fourier discretisation in azimuth and Chebyshev polynomials in radius (Trefethen 2000), with boundary conditions imposed following previous works (Nogueira & Edgington-Mitchell 2021), with the matrix operators detailled in Stavropoulos *et al.* (2023). A numerical mapping (Bayliss & Turkel 1992) is applied to ensure appropriate resolution in the shear layer of the jets. The sparsity of the system is exploited to further reduce computational cost. The mean flow uses a hyperbolic-tangent velocity profile (Michalke 1971) of the form

$$U(r) = M\left[0.5 + 0.5\tanh\left(\left(\frac{R_j}{r} - \frac{r}{R_j}\right)\frac{1}{2\delta}\right)\right], \tag{2.8}$$

with R_j the ideally expanded jet radius and δ used to characterise the shear-layer thickness. In each case, the mean temperature is obtained from 2.8 through the Crocco-Busemann relation. A twin-jet mean flow is constructed through the addition of two single-jet mean flows, following Rodríguez (2021). When considering instead an elliptical

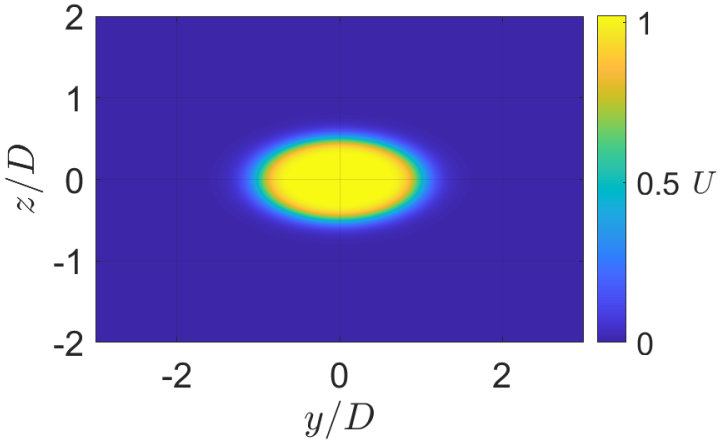

Figure 2: Sample elliptical jet mean flow, U, used for the finite-thickness model. Computed for $M_j = 1.16$, AR $= 2$, and $\delta = 0.2$.

geometry 2.8 is used with $R_j = R_b$, the boundary curve describing the ellipse

$$R_b = \frac{ab}{\sqrt{b^2 cos^2(\theta) + a^2 sin^2(\theta)}}. \tag{2.9}$$

Here b is the ellipse semi-minor axis, and a the semi-major axis as well as the length-scale used for normalisation. An example of a single elliptical jet mean flow using 2.9 and 2.8 is provided in figure 2, for an ideally expanded jet Mach number (M_j) of 1.16, $\delta = 0.2$ and aspect ratio (AR) of 2.

3. Results

3.1. *Planar twin jet*

To aid in understanding the behaviour of a round twin-jet system a planar twin-jet system, as described in §2.1, is considered first. For two jets being brought together to the point of merging, the simplified geometry of the planar case allows for a more intuitive understanding of the result. As the planar jets merge they are expected to form a singular planar jet, with width twice that of the individual planar jets. The effect on the structure of the pressure eigenfunction as the two jets merge ($H \to 1$) is shown in figures 3 and 4 for both the symmetric and anti-symmetric solutions respectively. In each case the wavenumber of the k_p^- $(0, 2)$ mode is found through 2.4. Both the symmetric and anti-symmetric solutions exhibit coupled behaviour in the inter-jet region even at higher ($H = 20$) jet separations. The primary difference observed between the symmetric (figure 3) and anti-symmetric (figure 4) eigenfunctions is the enforced symmetry condition at the midpoint of the system, which is consistent with results seen for a round twin-jet system Stavropoulos *et al.* (2023). It is observed in both cases that as H decreases the eigenfunctions appear to approach a higher-order mode shape, signified by additional anti-nodes in the pressure eigenfunction when $H = 1$ (figure 3(f) and figure 4(f)). As such, the system reduces to that of a single planar jet with half-width $2h$, referred to henceforth as the double-width jet. This higher-order mode the system reduces to for $H = 1$ is different depending on whether the symmetric or anti-symmetric solution is considered. In the symmetric case (figure 3) the amplitude at the midpoint between the jets increases with H before forming an anti-node. Conversely, the symmetry condition

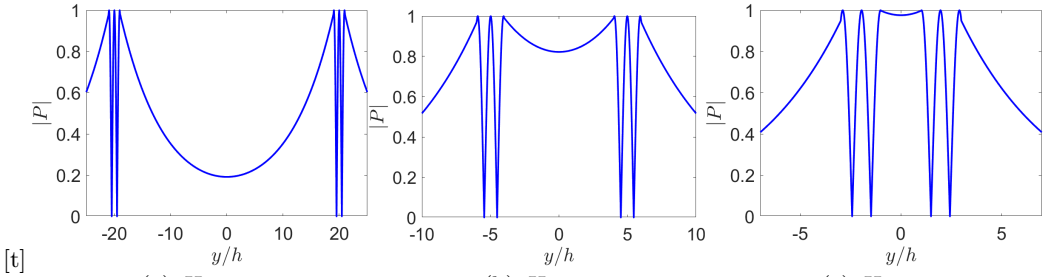

[t]

(a) $H = 20$ (b) $H = 5$ (c) $H = 2$

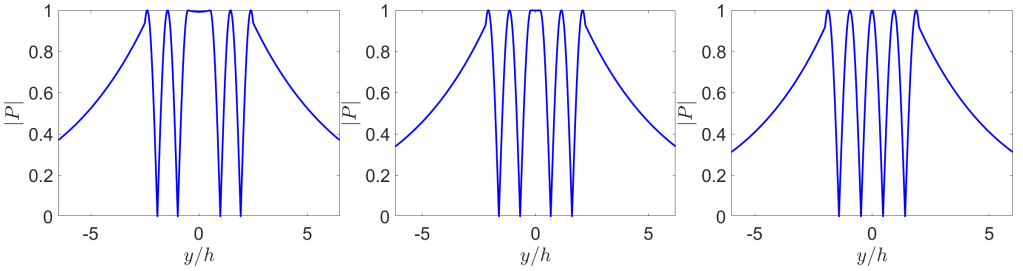

(d) $H = 1.5$ (e) $H = 1.2$ (f) $H = 1$

Figure 3: Variation in structure of the symmetric planar twin jet pressure eigenfunctions of the k_p^- $(0, 2)$ as the two jets merge $(H \to 1)$. Computed for, $M_j = 1.16$, $St = 0.25$ and T computed through an isentropic relation. Eigenfunctions are normalised with the absolute value plotted.

for the anti-symmetric case forces a node to form at the centre (figure 4). This results in the anti-symmetric case converging to a mode of even higher order than the symmetric case.

A more direct comparison between the twin-jet system at $H = 1$ and double-width jet can be seen in figure 5 for both the symmetric and anti-symmetric eigenfunctions. The solution for the double-width jet is found using the dispersion relation for a single planar jet, 2.5, but solved at a St twice that of the twin-jet case, due to the present formulation normalising by jet half-width which then becomes $2h$. For both the symmetric and anti-symmetric case in figure 5 the twin-jet solution matches exactly with the double-width jet confirming that the converged mode for $H = 1$ is a single-jet mode. A consideration of the eigenfunction behaviour of a planar twin-jet system as $H \to 1$ has identified key behaviours. When the planar twin-jet system merges it becomes equivalent to a single planar jet of twice the width. At this the point of merging $(H = 1)$ the pressure eigenfunction converges to a higher-order mode. For the symmetric case, as the two jets merge, a mode that previously had 3 peaks on each isolated jet forms a mode with 5 peaks in the merged jet $(H = 1)$. An equivalent mode for the anti-symmetric case forms a mode with 6 peaks, indicating the formation of a higher-order mode for this symmetry.

This convergence to the double-width jet solution of the twin jet as $H \to 1$ can also be observed when considering the branch and saddle point frequencies of the k_p^- (0,2) mode. It has been observed previously that the existence region formed by these bounds is strongly dependent on jet separation for a round twin-jet system (Du 1993; Stavropoulos *et al.* 2023) and this is also seen to be the case for a planar twin-jet system. Figure 6 shows the change in value of the branch and saddle points for both the symmetric and

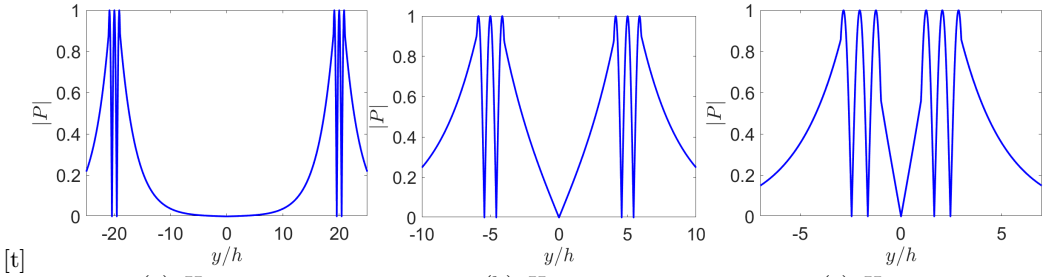

[t]

(a) $H = 20$ (b) $H = 5$ (c) $H = 2$

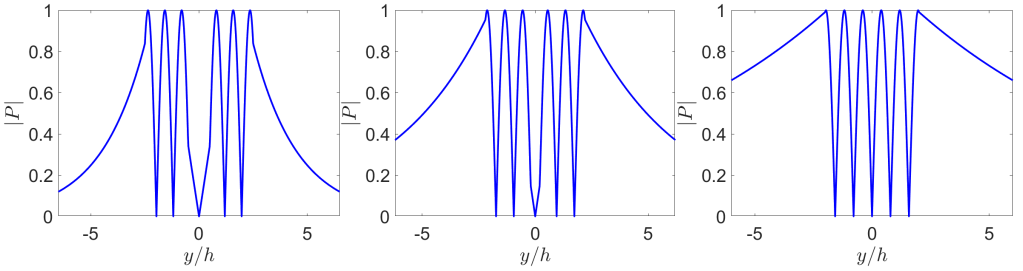

(d) $H = 1.5$ (e) $H = 1.2$ (f) $H = 1$

Figure 4: Variation in structure of the anti-symmetric planar twin jet pressure eigenfunctions of the k_p^- $(0, 2)$ mode as the two jets merge ($H \to 1$). Shown for, $M_j = 1.16$, T computed through an isentropic relation, and $St = 0.27$, (a) and (b), 0.29, (c), and 0.3, (d)-(f). Eigenfunctions are normalised with the absolute value plotted.

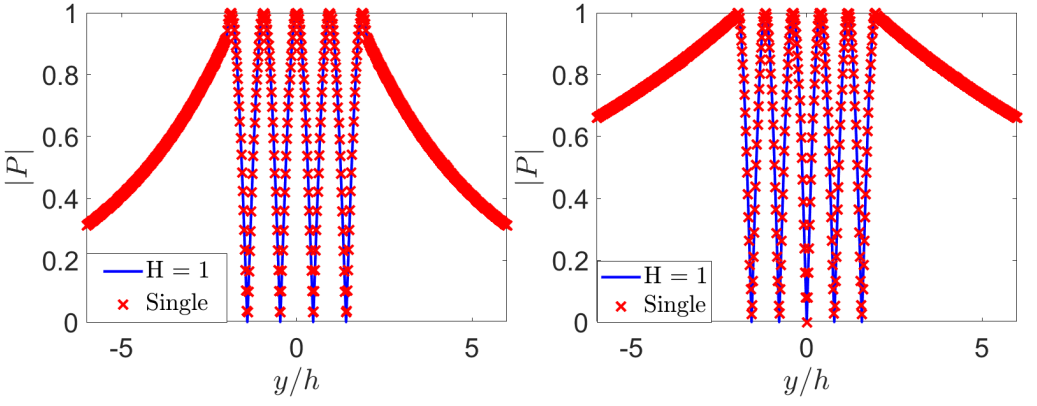

(a) *Symmetric* (b) *Anti − symmetric*

Figure 5: Eigenfunctions of the merged planar twin-jet system ($H = 1$) compared with those of the double-width single jet for both the symmetric solution, (a), and anti-symmetric solution (b). Shown for $M_j = 1.16$, and T computed through an isentropic relation. St values are 0.25 and 0.5 for (a), and 0.3 and 0.6 for (b), normalising using the twin and double-width jet length scales respectively.

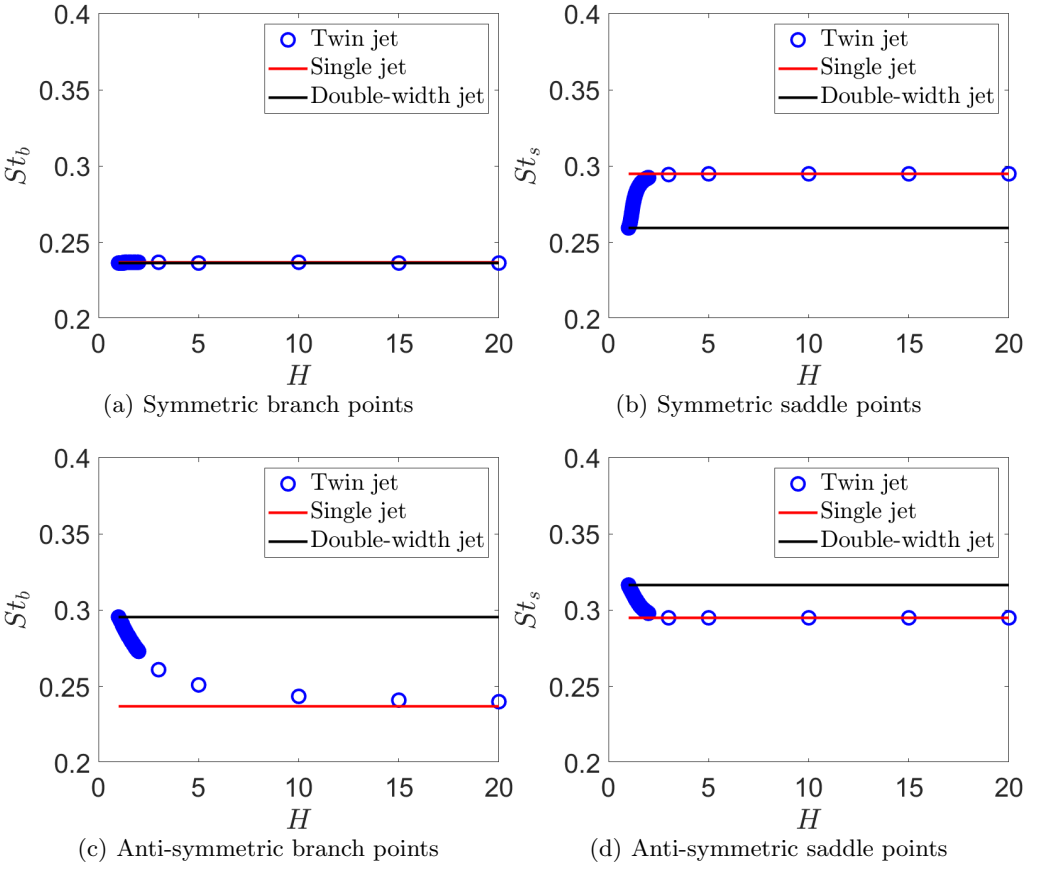

(a) Symmetric branch points (b) Symmetric saddle points

(c) Anti-symmetric branch points (d) Anti-symmetric saddle points

Figure 6: Branch and saddle points for the symmetric and anti-symmetric planar twin jet as a function of jet spacing H at $M_j = 1.16$ and T from an isentropic relation. Present also in each figure is the corresponding value of the symmetric single planar jet. St values converged to at $H = 1$ correspond to half those of the double-width jet.

anti-symmetric case. For both symmetries the branch and saddle point values are seen to begin (large H) from the value of the symmetric planar single jet. This is not unexpected when considering figure 3 and figure 4, where it can be observed that for large H the twin-jet eigenfunctions resemble two symmetric planar jets, with this also seen mathematically in Appendix B. As $H \to 1$ figure 6 shows the twin-jet branch and saddle points approach new values. The exception to this being figure 6(a), the symmetric solution saddle point, which remains virtually unchanged for all H. These new values the branch and saddle points converge to are all related to the double-width jet, being exactly half the values of the double-width jet branch and saddle points. Recalling that an equivalent double-width jet has St twice that of a planar twin jet, then figure 6 is indicating that when the twin-jet system merges ($H = 1$) the branch and saddle points change to match those of the higher-order mode the system has now converged to.

The entire existence region of the k_p^- (0,2) mode is compared in figure 7 between the twin-jet system and the double-width jet, with the twin-jet values scaled to match the double-width jet normalisation. These are plotted for $M_j = 1.16$, $H = 1$ and an isentropic temperature ratio. Both twin and double-width jet are seen to exhibit exact agreement in

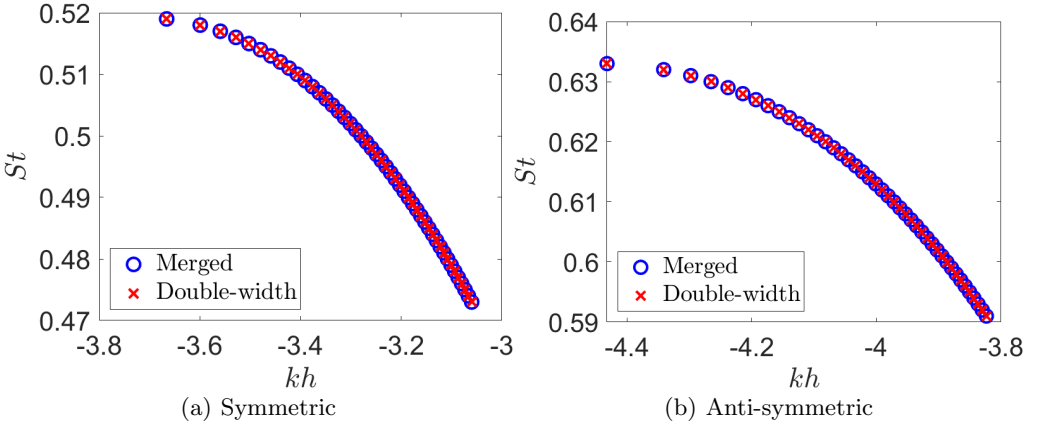

(a) Symmetric (b) Anti-symmetric

Figure 7: Comparison between the k_p^- (0,2) existence region between the planar twin jet ($H = 1$) and double-width jet for symmetric, (a), and anti-symmetric, (b). Computed for M_j 1.16 and T from an isentropic relation. The twin-jet eigenvalues have been scaled by a factor of two to adjust them to the double-width jet normalisation.

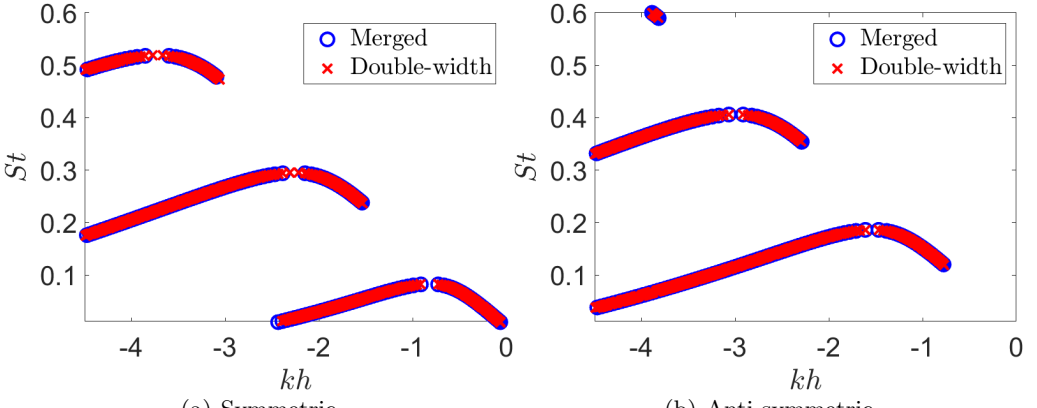

(a) Symmetric (b) Anti-symmetric

Figure 8: Comparison of (kh, St) eigenvalue pairs between the planar twin jet ($H = 1$) and double-width jet for symmetric, (a), and anti-symmetric, (b). Computed for M_j 1.16 and T from an isentropic relation. The twin-jet eigenvalues have been scaled by a factor of two to adjust them to the double-width jet normalisation.

the symmetric, figure 7(a), and anti-symmetric, figure 7(b), cases. This agreement is to be expected as the twin-jet system is forced to match the double-width jet as $H \to 1$, a criterion imposed by the pressure eigenfunction behaviour. This constraint then forces the branch and saddle points (and consequently, the existence region) of the k_p^- $(0, 2)$ mode to align with the higher-order mode of the double-width jet the system has converged to. A change in branch or saddle point will only not occur if the value already corresponds to that of the double-width jet, as seen for the symmetric branch point in figure 6(a). A larger range in St is considered in figure 8, for the same jet parameters as in figure 7. This demonstrates that the results observed thus far for the k_p^- $(0, 2)$ mode in a planar jet, hold for other modes also. These modes also converge to the double-width jet solution as

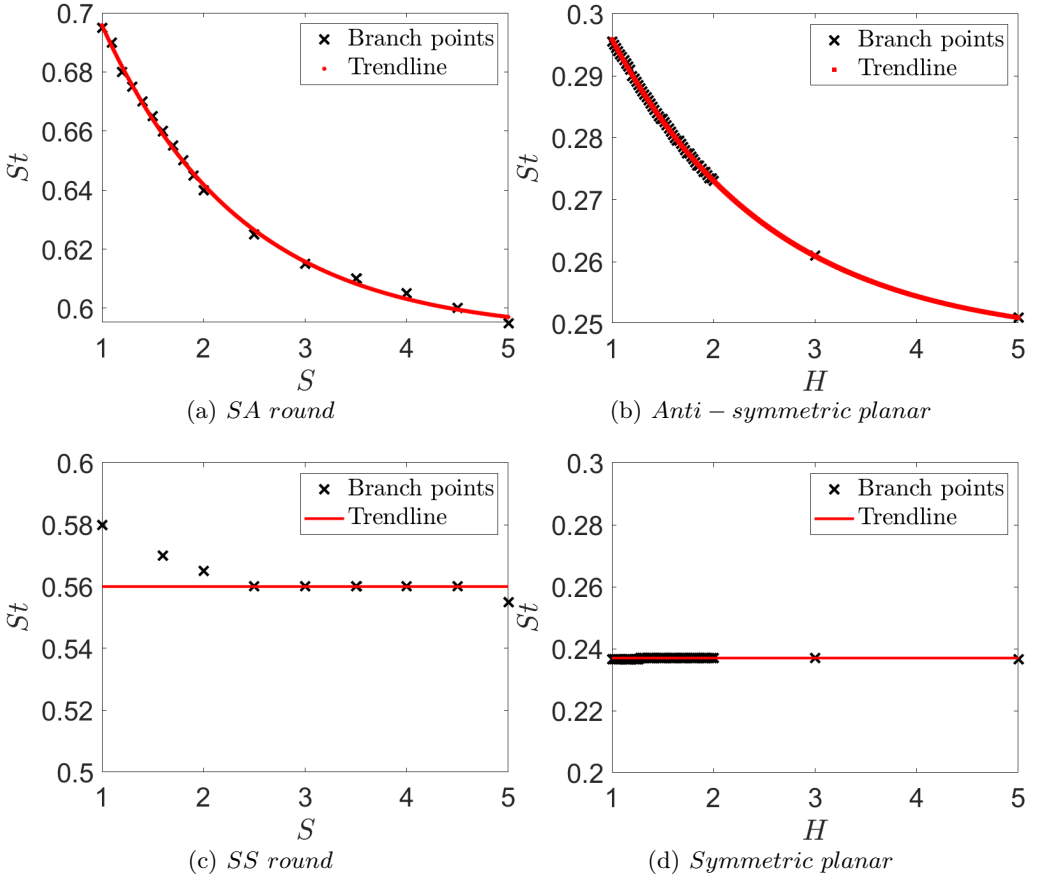

Figure 9: Dependence of the k_p^- $(0,2)$ branch point with jet separation for both the SA (a) and SS (c) round twin jet, and the anti-symmetric (b) and symmetric (d) planar twin jet. Computed for $M_j = 1.16$ and $\delta = 0.2$ (round twin jet). Overlaid on (a) and (b) is an exponential trendline, with a constant trendline on (c) and (d).

$H \to 1$, and will experience changes in their branch and saddle point values with H to align with the double-width jet solution. This explanation for the k_p^- $(0,2)$ mode branch and saddle point behaviour in a planar twin-jet system now motivates the investigation of the round twin-jet system.

3.2. *Round twin jet*

For the round twin-jet system it has been seen previously that the SA symmetry k_p^- $(0,2)$ mode, exhibits a strong dependence on jet separation (Stavropoulos *et al.* 2023). The behaviour of both the SS and SA symmetry round twin-jet branch points are compared to those of the symmetric and anti-symmetric planar twin-jet system in figure 2.7. Results for the round twin-jet system are obtained using 2.7 and 2.8 with $\delta = 0.2$. In the SA (figure 9(a)) and anti-symmetric (figure 9(b)) systems the branch points both exhibit a strong exponential trend as the jets are brought together. A similar agreement in trends can be seen between the SS (figure 9(c)) and symmetric (figure 9(d)) branch points. Here the branch points exhibit a constant trend with jet separation and only at very low jet separations is there a change (being at lower jet separation than

previous considerations of the SS k_p^- $(0, 2)$ mode Du (1993); Stavropoulos *et al.* (2023)) which is greater for the SS round twin jet than the symmetric planar twin jet. The similarity in trends of figure 9 suggests that the round twin-jet system is also converging to an equivalent geometry when $S = 1$ driving this change in branch point frequency. The behaviour of the round twin-jet pressure eigenfunctions can then also be considered, as $S \to 1$. These are presented in figure 10 for the SA symmetry at $M_j = 1.16$ and $\delta = 0.2$. As the two round jets are brought together the SA symmetry condition enforced at the system midpoint becomes an additional node as part of a higher-order mode. This is the same behaviour as was observed previously for the anti-symmetric planar twin-jet system (figure 4). The eigenfunction behaviour of the SS symmetry can also be considered and is illustrated in figure 11. Here the SS symmetry condition enforced at the system midpoint becomes an anti-node and the twin-jet system reduces to a higher-order mode, again in-line with observations of the planar twin jet (figure 5). Comparing the SS and SA eigenfunctions at $S = 1$ (figures 10(d) and 11(d)) the same difference as previously identified for the planar twin-jet system (§3.1) is observed, the SA solution converges to an even higher-order mode than the SS solution. Figures 10 and 11 further indicate that the round twin-system is converging to some equivalent geometry.

The geometry of a round twin-jet system does not lend itself to an obvious equivalent geometry when the two jets merge, unlike the planar twin-jet system discussed previously (§3.1). Instead a comparison will be made with ellipses of differing AR. The two ARs considered are 1.5 and 2, with each shown superimposed over the $S = 1$ round twin-jet system in figure 12. The AR 1.5 case (figure 12(a)) provides a match with the outer edges of the two jets, whilst the AR 2 case (figure 12(b)) is an ellipse of equal area to the twin-jet system. The $S = 1$ SA round twin-jet existence region is compared to (k, St) pairs computed for the elliptical jet, using 2.9 to define the mean flow boundary, in figure 13. Here $M_j = 1.16$ and $\delta = 0.2$, with $\mu = 0$, 1 for the ellipse and $S = 1$ for the twin jet. In figure 13 both the St and k values for the round twin-jet system are scaled by a factor of $\sqrt{\frac{AR}{2}}$ to use the same normalisation as the ellipse. It can be seen that of the ARs considered, the merged round twin-jet system more closely resembles the AR 2 ellipse (figure 13 (b) and (d)). This is evident from the close agreement observed at the region near the branch point, and the similar behaviour of the twin jet and elliptical jet mode branches. Conversely in the AR 1.5 case (figure 13(a) and (c)) the existence regions for the elliptical and round twin jet do not show alignment. Note that this is not implying that a round twin-jet system converges to a perfect ellipse, but that an AR 2 ellipse could be considered a close approximation to the resultant converged geometry. Considering now just the AR 2 case, comparisons between the pressure eigenfunctions for the ellipse and round twin jet can be made to further consider the similarities. These are given in figure 14 at the branch point, for the radial profile along the y axis (figures 14(a) and (b)), and the pressure contours (figure 14(b)-(d)). In figure 14(a) the shape of the eigenfunctions agree well between the elliptical and twin-jet solutions. The difference between the $\mu = 1$ ellipse and SA round twin jet is in the eigenfunction amplitudes, with the first and third nodes having greater magnitude for the ellipse than the round twin jet. When considering instead the $\mu = 0$ ellipse and SS round twin jet (figure 14(b)) a greater degree of difference is observed between the two eigenfunctions. For $y/D > 1$ the elliptical eigenfunction decays at a slower rate than the twin-jet eigenfunction, and at $y/D = 0$ there is disagreement seen between the two. Comparing the pressure contours for the $\mu = 1$ ellipse and SA round twin jet (figures 14(c) and (d)) indicates a similar location for the maximum pressure with differences in the contours occurring outside of this region. This is similarly observed when comparing the $\mu = 0$ ellipse and SS round

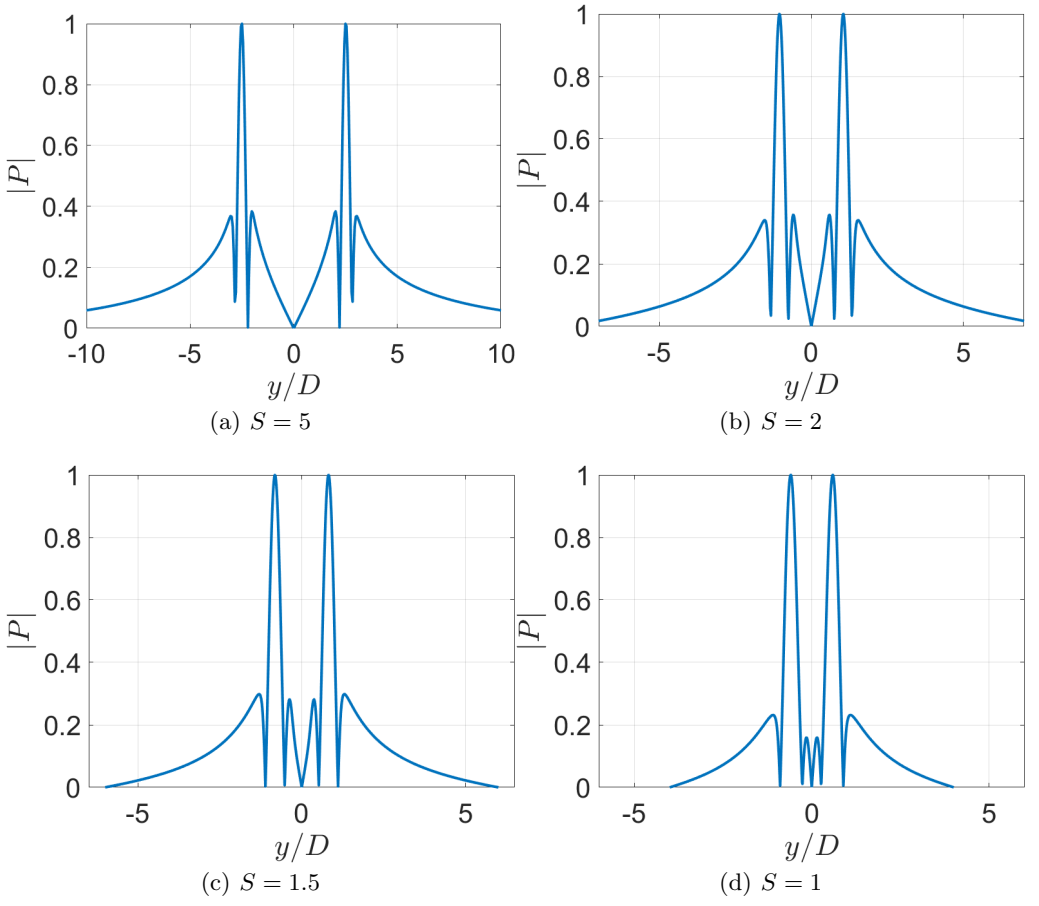

Figure 10: Variation in structure of the SA round twin jet pressure eigenfunctions of the k_p^- $(0, 2)$ mode as the two jets merge ($S \to 1$). Computed for, $M_j = 1.16$ and $\delta = 0.2$. Values of St are 0.595 (a), 0.64 (b), 0.665 (c), and 0.695 (d). Eigenfunctions are normalised with the absolute value plotted.

twin jet (figures 14(e) and (f)). In both cases greater differences between the elliptical and twin-jet contours are seen near to the z axis (larger values of θ as described by figure 1(b)). This result is consistent with comparisons of mean flow velocity profiles between the ellipse and $S = 1$ round twin jet (see Appendix C), where it observed that differences between the velocity profiles occur for large values of θ. Trends in the pressure eigenfunction radial profiles, from branch point to saddle point are compared in figure 15. For the SA round twin jet (figure 15(a)) and $\mu = 1$ ellipse (figure 15(b)) both are seen to display similar behaviour in the pressure eigenfunction as St increases towards the saddle point value. Differences between the two geometries are observed in the pressure eigenfunction amplitudes and the profile at the saddle point. When considering the SS round twin jet (figure 15(c)) and $\mu = 0$ ellipse (figure 15(d)) similar agreement between the geometries is observed, however at $y/D = 0$ the SS twin jet increases in amplitude as St increases to a larger extent than the $\mu = 0$ ellipse does. Combined figures 14 and 15, like figure 13, indicate that the equivalent geometry a round twin-jet system merges to is close in shape to an AR 2 ellipse.

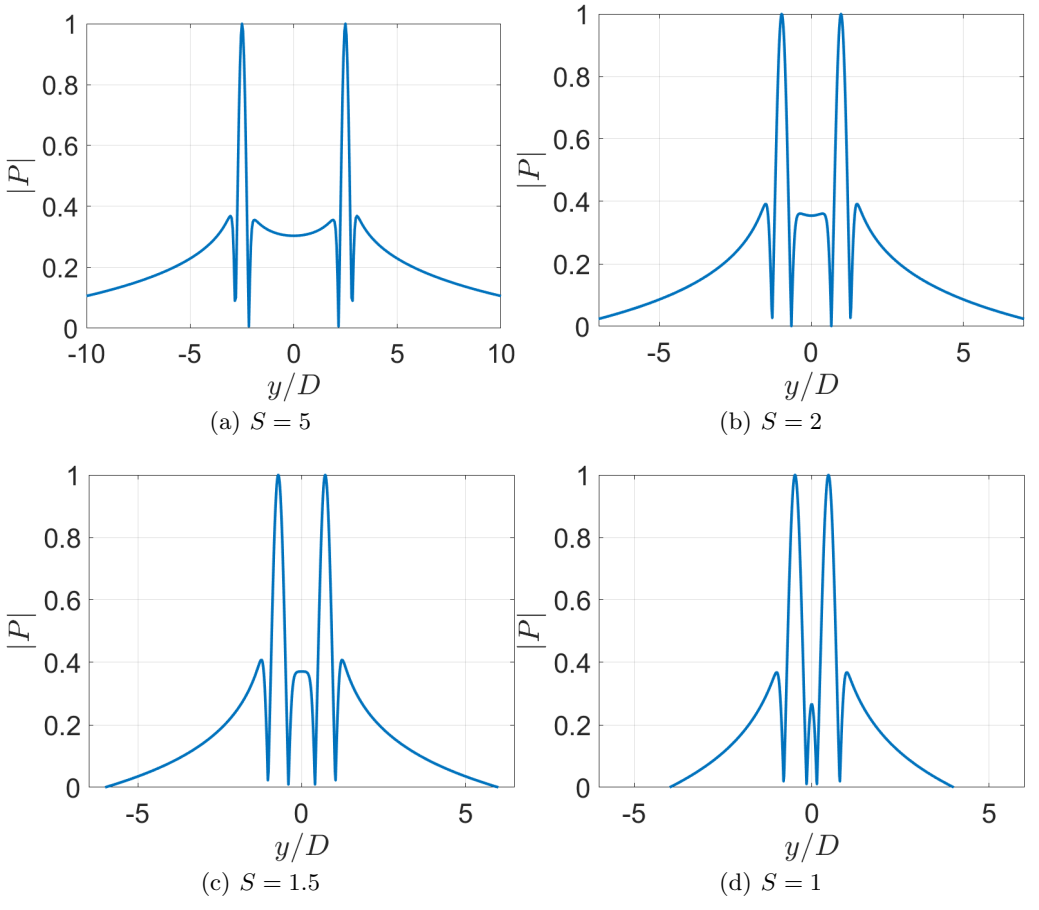

Figure 11: Variation in structure of the SS round twin jet pressure eigenfunctions of the k_p^- $(0, 2)$ mode as the two jets merge ($S \to 1$). Computed for, $M_j = 1.16$ and $\delta = 0.2$. Values of St are 0.555 (a), 0.565 (b), 0.57 (c), and 0.58 (d). Eigenfunctions are normalised with the absolute value plotted.

4. Conclusion

This work sought to explain the strong observed dependence of the k_p^- $(0, 2)$ with jet separation in a twin-jet system. A planar twin-jet model was first considered due to the simplified geometry it provided. The model demonstrated that as the two jets are brought together a higher-order mode is formed, for a single-jet system of twice the jet width. This then imposes a constraint on the branch and saddle point frequencies of the k_p^- $(0, 2)$ to match those of the higher-order mode branch. To meet this constraint the values must then change with jet separation, leading to the previous observations of jet separation dependence. The symmetry condition of the system, symmetric or anti-symmetric, influences the shape of the higher-order mode that is formed. An anti-symmetric system leads to a greater order mode than a symmetric system, and so results in a greater change in branch and saddle point values. The same behaviour was observed also for the round twin-jet system which converges to an equivalent geometry similar to an AR 2 ellipse. A higher-order mode similar to that of an elliptical jet was formed as the jets were brought together, with the existence region of the k_p^- $(0, 2)$ mode then

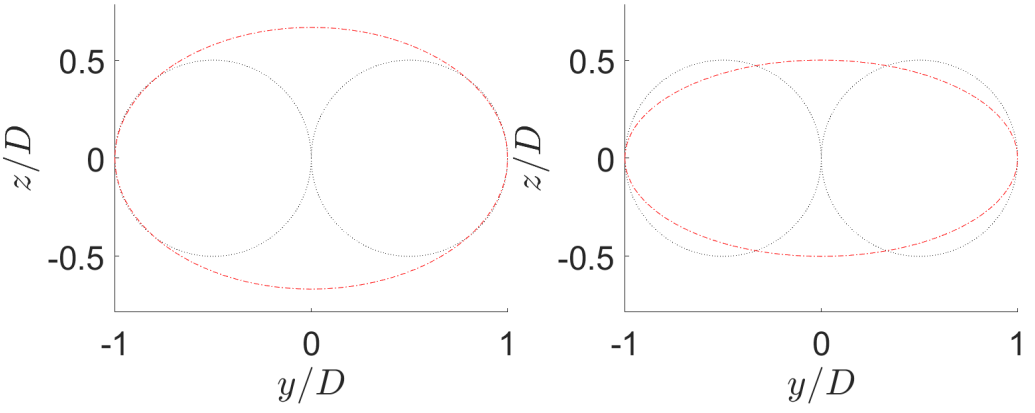

(a) $AR = 1.5$ (b) $AR = 2$

Figure 12: Geometric comparison between the $S = 1$ round twin-jet system and an elliptical jet of AR 1.5 (a), and 2 (b).

constrained to match. As this k_p^- $(0, 2)$ mode behaviour is due to a geometric effect, in converging to an equivalent single-jet geometry as the individual jets merge, such behaviour will be observed in any twin-jet system.

This work was supported by the Australian Research Council under the Discovery Project Scheme: DP190102220. M. N. Stavropoulos is supported through an Australian Government Research Training Program Scholarship. Computational facilities supporting this project include the Multi-modal Australian ScienceS Imaging and Visualisation Environment (MASSIVE). Figures in Appendix A make use of the colourmaps in the CMasher package (van der Velden 2020).

Appendix A. Variation with jet parameters

This work has focused on the behaviour of the k_p^- $(0, 2)$ mode with S and solution symmetry. Here consideration is made for how other jet parameters (M_j and T) affect the branch point St value for a round twin-jet system. In each case the value considered will be St_r which is defined as the ratio between the round twin-jet St value and the equivalent round single-jet St value for the same jet conditions. Calculations here use the round twin-jet vortex-sheet model (Morris 1990; Du 1993; Stavropoulos *et al.* 2022), as the lower computational cost facilitates a wider parameter space exploration. The dispersion relation for the round twin jet is

$$\sum_{m=0}^{\infty} A_m[a_{nn}\delta_{mn} \pm (-1)^m c_{mn}] = 0, \tag{A 1}$$

with

$$a_{nn} = \frac{1}{(1-\frac{kM}{\omega})^2} - \frac{1}{T}\frac{\lambda_o}{\lambda_i}\frac{K_n'(\frac{D_j\lambda_0}{2})I_n(\frac{D_j\lambda_i}{2})}{I_n'(\frac{D_j\lambda_i}{2})K_n(\frac{D_j\lambda_0}{2})}, \tag{A 2}$$

and

$$c_{mn} = (-1)^n\epsilon_n[K_{m-n}(\lambda_0 S)\pm K_{m+n}(\lambda_0 S)]\left[\frac{I_n(\frac{D_j\lambda_0}{2})}{K_n(\frac{D_j\lambda_0}{2})}\frac{1}{(1-\frac{kM}{\omega})^2} - \frac{1}{T}\frac{\lambda_o}{\lambda_i}\frac{I_n(\frac{D_j\lambda_i}{2})I_n'(\frac{D_j\lambda_0}{2})}{K_n(\frac{D_j\lambda_0}{2})I_n'(\frac{D_j\lambda_i}{2})}\right]. \tag{A 3}$$

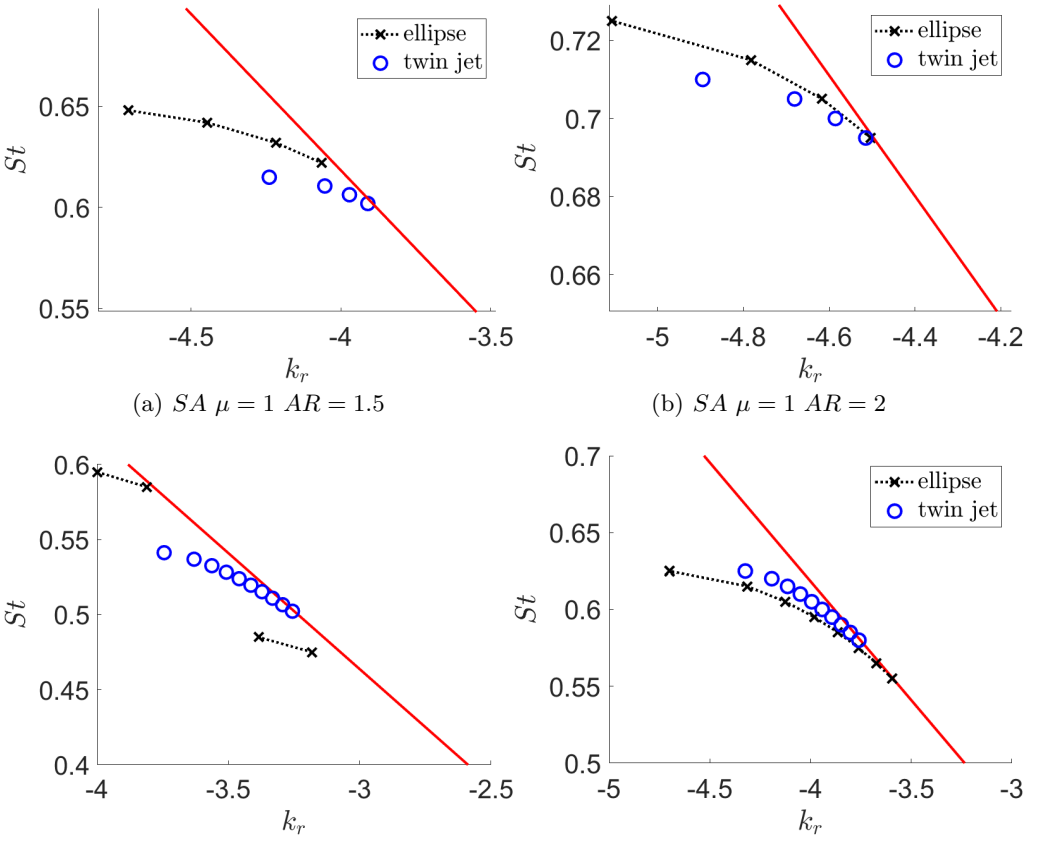

(a) $SA\ \mu = 1\ AR = 1.5$ (b) $SA\ \mu = 1\ AR = 2$

(c) $SS\ \mu = 0\ AR = 1.5$ (d) $SS\ \mu = 0\ AR = 2$

Figure 13: Comparison of the existence regions of the SS and SA $S = 1$ round twin-jet k_p^- $(0, 2)$ mode and the $\mu = 0$, 1 elliptical jet mode branch it lies closest to. Computed for $M_j = 1.16$, $\delta = 0.2$, and AR = 1.5 (a), (c) and 2 (b), (d). Values of St for the twin-jet system are scaled to match the normalisation of the elliptical St. Included also is the sonic line representing the free-stream acoustic waves in red.

Here I_n and K_n are the modified Bessel functions of first and second kind, δ_{mn} is the Kronecker delta, $\epsilon_n = 0.5$ for n = 0 and $\epsilon_n = 1$ otherwise, m the azimuthal mode number, and the $\pm$ terms in A 1 and A 3 describe the solution being symmetric $(+)$ or anti-symmetric $(-)$ about the $x - y$ and $x - z$ planes respectively. All other parameters are as described previously for the planar vortex-sheet model (§2.1). Using A 1, contours describing the change in St_r across M_j are presented for the SA solution symmetry in figure 16 for different values of the temperature ratio T. Across the values of T considered the same trend is observed. The SA branch point Sts are of larger value than the single jet at lower S, and move towards the single-jet value as S increases. As T is increased it results in the twin-jet values approaching those of the single jet sooner with increasing S. It is only in figure 16(a) that a dependence on M_j can be seen. However this result uses an isentropic temperature relation for T, which is dependent on M_j. As such it can be stated that M_j does not influence the behaviour of the SA symmetry twin-jet branch points relative to those of the single jet. A final comparison is shown in figure 17 for all four solution symmetries of a twin-jet system, SS, SA, AS and AA. As the AS and

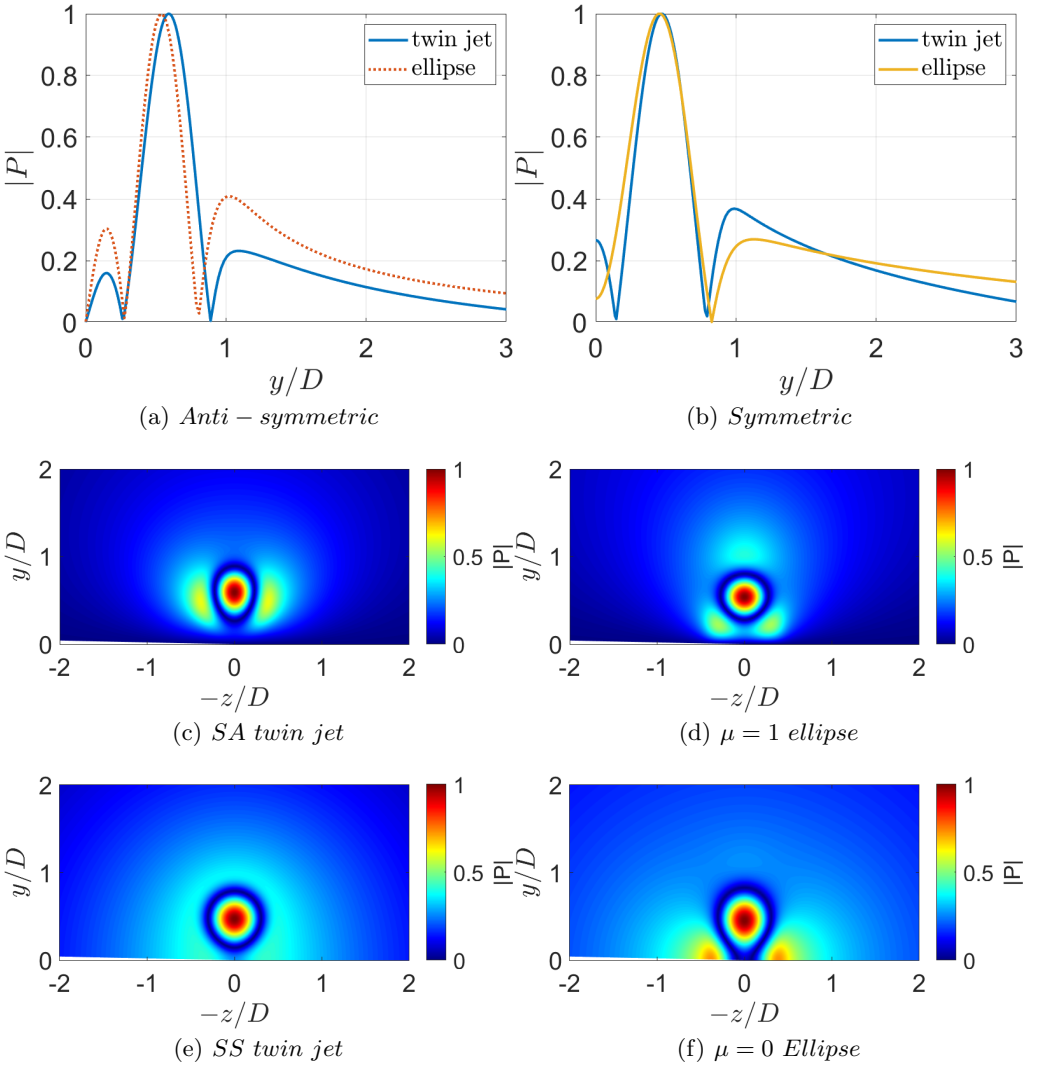

Figure 14: Pressure eigenfunctions of the $\mu = 0$ and 1 ellipses, and the SS and SA $S = 1$ round twin jet computed at the branch point. Shown for the radial profile (a) and (b), anti-symmetric contours (c) and (d), and symmetric contours (e) and (f). Computed for $M_j = 1.16$, and $\delta = 0.2$. Eigenfunctions are normalised with the absolute value plotted.

AA symmetries cannot support axisymmetric modes, by construction, the behaviour of the k_p^- $(1, 1)$ mode will be considered instead. Comparing figure 17(b) with figure 16(a) highlights that the $(1, 1)$ mode reaches the single-jet value sooner with increasing S than the $(0, 2)$ mode. Indicating that as the round twin-jet system merges ($S \to 1$) the different modes of the jet all converge to higher-order modes at different rates. Comparing the behaviours of the different symmetries it is seen that the SS and AS symmetries (figure 17(a) and (c)) and the SA and AA symmetries (figure 17(b) and (d)) display similar behaviour. The SS and AS symmetries branch point values decrease from the single-jet value as S decreases, whilst the SA and AA symmetry branch points increase in value. The difference between the two groupings of symmetry is their symmetry or anti-

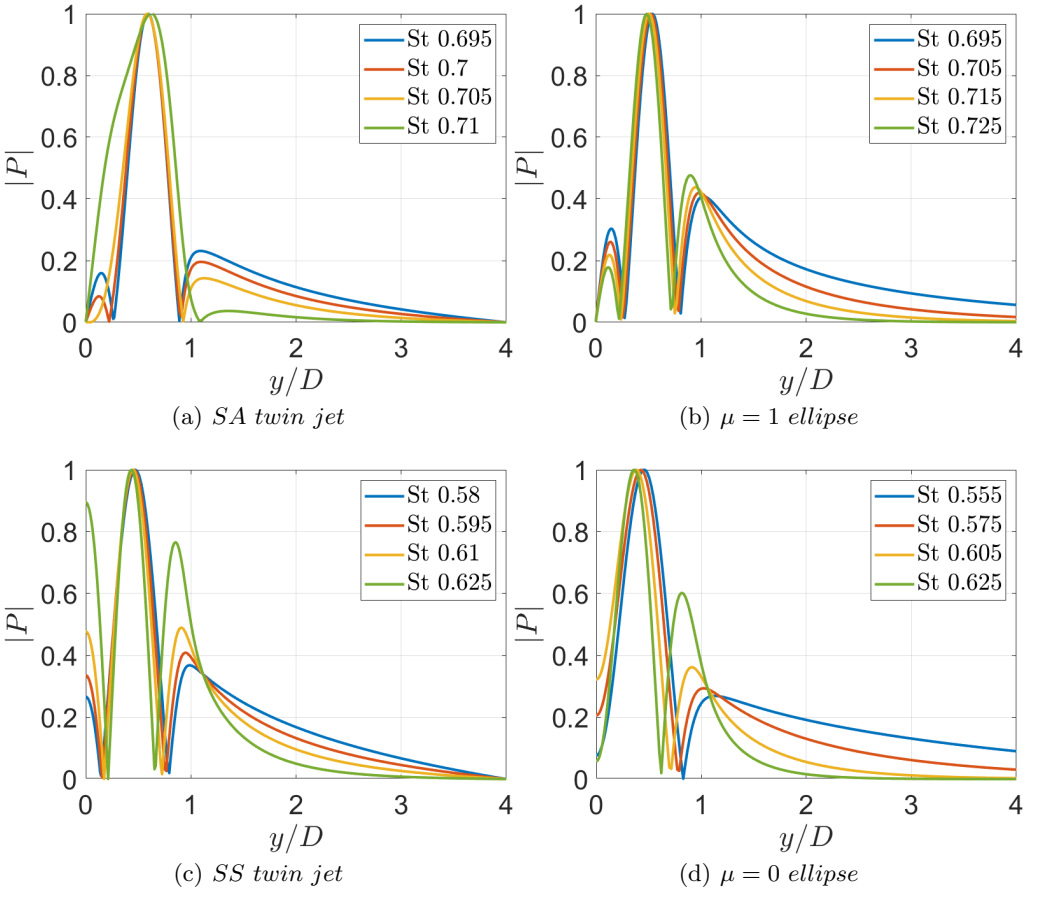

(a) *SA twin jet* (b) $\mu = 1$ *ellipse*

(c) *SS twin jet* (d) $\mu = 0$ *ellipse*

Figure 15: Comparison of the pressure eigenfunction behaviour between the $S = 1$ round twin jet, (a) and (c), and the AR 2 ellipse, (b) and (d), when moving from the branch to saddle point. Computed for $M_j = 1.16$, $\delta = 0.2$, and AR $= 2$. Eigenfunctions are normalised with the absolute value plotted along the y axis.

symmetry about the $x - z$ plane. In §3.2 it was observed that the SS and SA symmetries converge to a geometry similar to an AR 2 ellipse with symmetry or anti-symmetry about the $x - z$ plane. Hence, figure 17 is indicating that the higher-order mode the k_p^- $(1, 1)$ mode converges to exists at a higher St range for the equivalent geometry the SA and AA symmetries converge to, than for the equivalent geometry of the merged SS and AS symmetries.

Appendix B. Matrix terms for the planar model

In the planar twin-jet model the flow can be divided into three distinct regions. These are; the region between the jets $(-H < y < h)$, the region inside the jet $(-h < y < h)$, and the region away from the other jet $(y > h)$. Using 2.2 the pressure in each of the

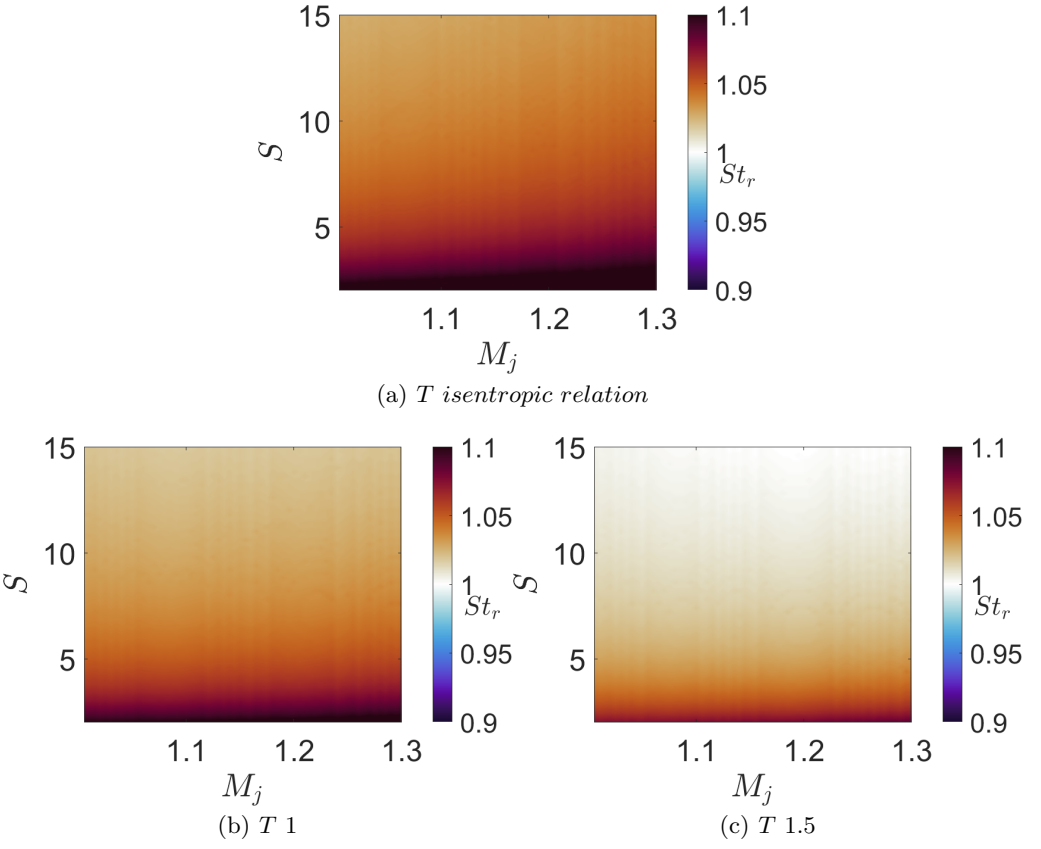

(a) T *isentropic relation*

(b) T 1

(c) T 1.5

Figure 16: Variation in the ratio of the SA round twin-jet k_p^- $(0, 2)$ branch point and the single-jet equivalent, across S and M_j. Computed for T using an isentropic relation (a), $T = 1$ (b), and $T = 1.5$ (c).

regions can be written as

$$\begin{aligned} P(y) &= C_1 e^{\lambda_o y} + C_2 e^{-\lambda_o y} \quad -H < y < -h, \\ P(y) &= C_3 e^{\lambda_i y} + C_4 e^{-\lambda_i y} \quad -h < y < h, \\ P(y) &= C_5 e^{\lambda_o y} + C_6 e^{-\lambda_o y} \quad y > h. \end{aligned} \tag{B 1}$$

The requirement for the pressure to be bounded dictates that C_5 must be zero. Imposing the symmetry boundary condition at $y = -H$ yields a relation between C_1 and C_2, allowing the pressure in the inter-jet region to be re-written as

$$P(y) = C_1 \left(e^{\lambda_o y} \pm e^{-2H\lambda_0} e^{-\lambda_o y} \right), \tag{B 2}$$

where it can be noted that for sufficiently large H the single-jet solution is recovered. Applying this to B 1 yields the eigenvalue problem described by 2.4 where,

$$\boldsymbol{A} = \begin{bmatrix} e^{-\lambda_o} \pm e^{-2H\lambda_0} e^{\lambda_o} & -e^{-\lambda_i} & -e^{\lambda_i} & 0 \\ \frac{\lambda_o}{\omega^2} \left(e^{-\lambda_o} \mp e^{-2H\lambda_0} e^{\lambda_o} \right) & \frac{-\lambda_i e^{-\lambda_i}}{\frac{1}{T}(kM-\omega)^2} & \frac{\lambda_i e^{\lambda_i}}{\frac{1}{T}(kM-\omega)^2} & 0 \\ 0 & -e^{\lambda_i} & -e^{-\lambda_i} & e^{-\lambda_0} \\ 0 & \frac{\lambda_i e^{\lambda_i}}{\frac{1}{T}(kM-\omega)^2} & \frac{-\lambda_i e^{-\lambda_i}}{\frac{1}{T}(kM-\omega)^2} & \frac{\lambda_0}{\omega^2} e^{-\lambda_0} \end{bmatrix}, \tag{B 3}$$

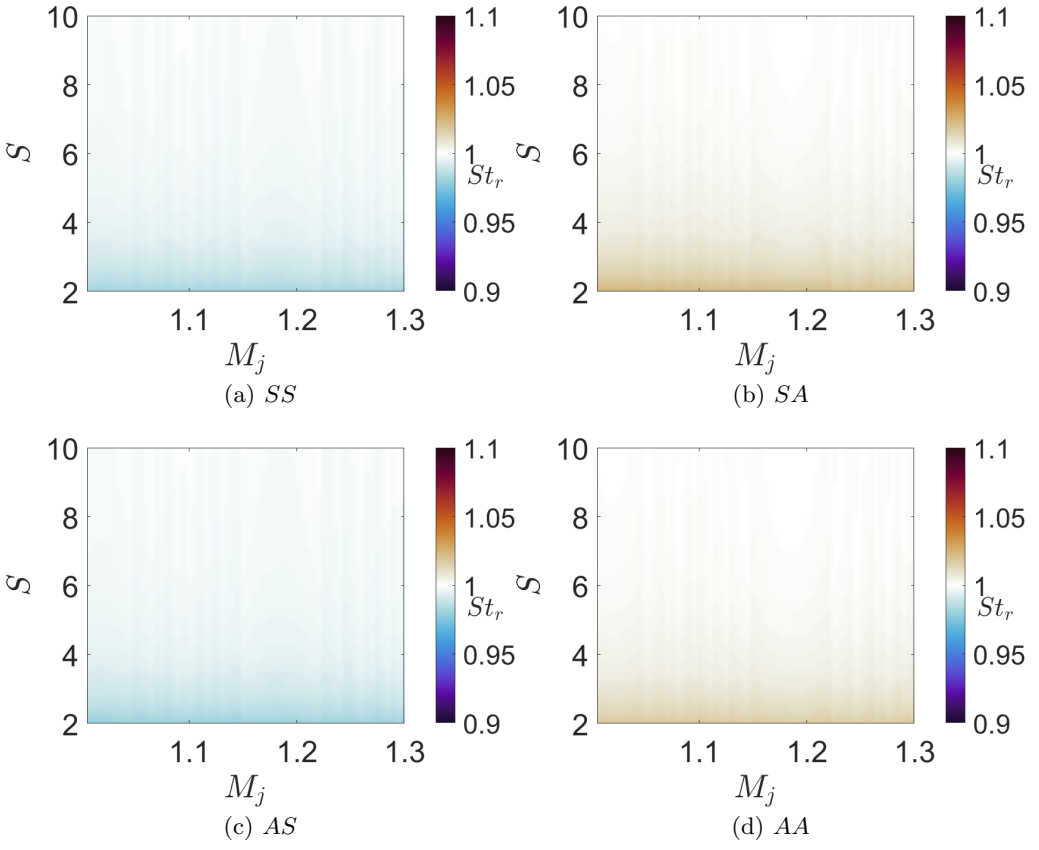

(a) *SS* (b) *SA*

(c) *AS* (d) *AA*

Figure 17: Variation in the ratio of the round twin-jet k_p^- $(1,1)$ branch point and the single-jet equivalent, across S and M_j. Computed using an isentropic relation for T and for SS (a), SA (b), AS (c), and AA (d) solution symmetry.

and

$$\boldsymbol{c} = \begin{bmatrix} C_1 \\ C_3 \\ C_4 \\ C_6 \end{bmatrix}. \tag{B 4}$$

Appendix C. Comparison of velocity profiles

Additional detail is provided on the differences between the elliptical jet mean flow and the merged round twin-jet mean flow. Both mean flows are illustrated in figure 18 for the elliptical (a), and round twin jet (b) respectively. These are computed for $M_j = 1.16$, $\delta = 0.2$, AR $= 2$ (ellipse), and $S = 1$ (round twin jet). A qualitative view of figure 18 indicates that the two mean flows are quite different, particularly in their respective behaviour close to the z axis. A more quantitative comparison is made in figure 19 where the velocity profiles are compared along multiple angles, θ, measured from the y axis (see figure 1(b)). For lower θ (figure 19(a)-(d)) there is strong agreement observed between the two mean flows. It is only at larger θ (figure 19(e) and (f)) that the two mean flows display noticeable difference. As such, this provides a strong justification for considering

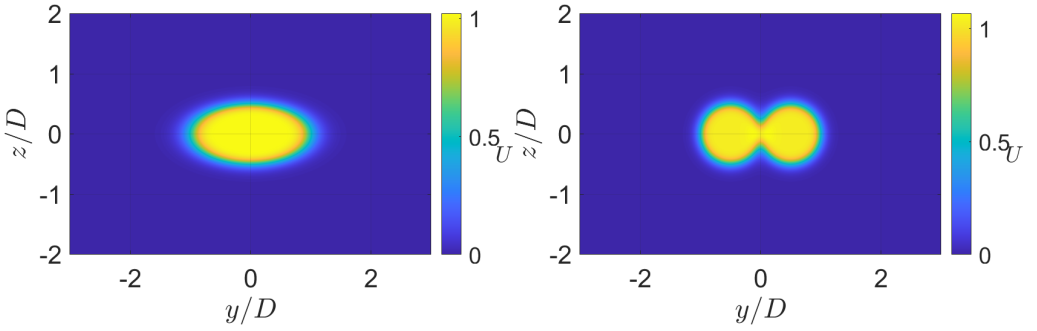

Figure 18: Visual comparison of the mean flows for an AR 2 ellipse, (a), and $S = 1$ twin jet, (b). Computed for $M_j = 1.16$ and $\delta = 0.2$

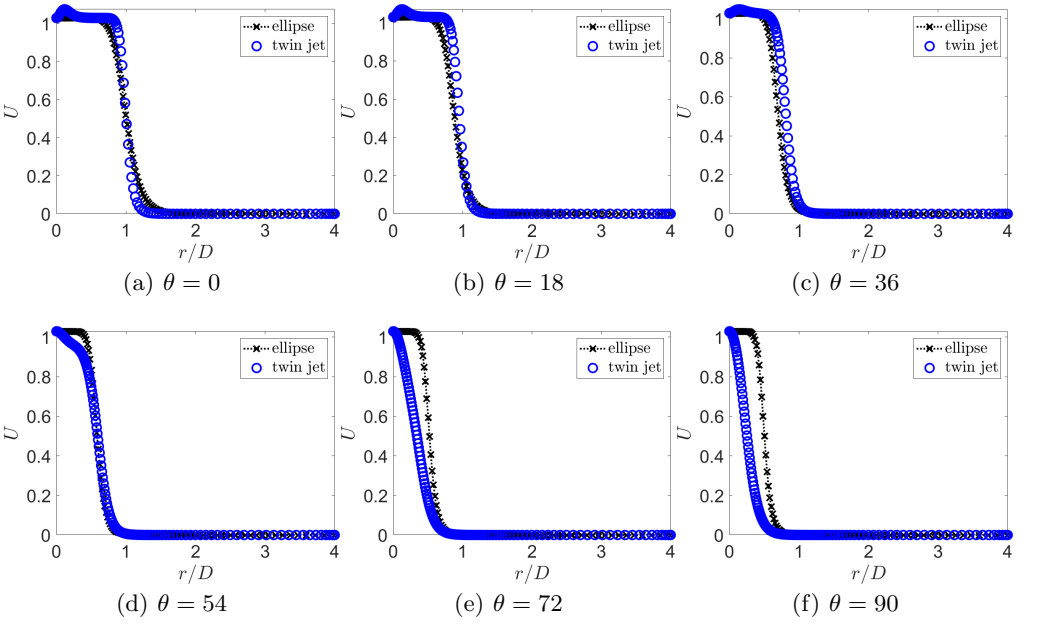

Figure 19: Comparison of mean flow axial velocity profiles between the AR 2 ellipse and $S = 1$ twin jet. Computed for $M_j = 1.16$, $\delta = 0.2$ at θ of 0, (a), 18, (b), 36, (c), 54, (d), 72, (e), and 90, (f), all measured from the positive y axis.

an AR 2 ellipse as a substitute for the equivalent geometry of a merged round twin-jet system.

Appendix D. Formulation for an N-jet planar system

In this work a planar twin-jet vortex-sheet model was described extending the planar single-jet vortex-sheet model previously considered (Martini *et al.* 2019). Here the formulation is generalised even further for a system of n planar jets each separated by a distance $2H$, where $n \geqslant 1$. In a system of n jets each jet is described using 2 vortex

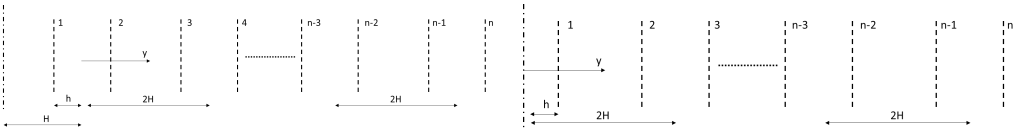

(a) Even n (b) Odd n

Figure 20: Set-up of the planar n-jet system for both an even, (a), and odd, (b), number of jets.

sheets, one for each jet boundary, resulting in a total of $2n$ vortex sheets. As was done for the twin planar jet (§2.1) the system of n jets will be divided in two with either a symmetric or anti-symmetric condition applied at the midpoint, leaving only n vortex sheets to consider. This set-up is illustrated in figure 20. To begin, the formulation for a symmetric solution is considered (figure 20(a)). The n vortex sheets result in $n+1$ flow regions. These regions may be inside or outside of a jet and have a general form for the perturbed pressure amplitudes following 2.2, where $a < b$. This results in $2n+2$ unknown coefficients, requiring the same number of boundary conditions to solve. Two boundary conditions are obtained through applying the symmetry condition at $y = -H$, and imposing the solution to be bounded as $y \to \infty$. The remaining $2n$ boundary conditions arise from applying continuity of pressure and displacement across each of the n vortex sheets. Each value A_{uv} of $\mathbf{A}$, in 2.4, is defined as the term multiplying the coefficient C_v as follows,

$$e^{-\lambda_o H} C_1 \mp e^{\lambda_o H} C_2 = 0, \tag{D 1}$$

for $u = 1$,

$$e^{\lambda_o(\frac{u-2}{4}(2H)-1)} C_{v-1} + e^{-\lambda_o(\frac{u-2}{4}(2H)-1)} C_v - e^{\lambda_i(\frac{u-2}{4}(2H)-1)} C_{v+1} - e^{-\lambda_i(\frac{u-2}{4}(2H)-1)} C_{v+2} = 0, \tag{D 2}$$

for even u and odd $\frac{u}{2}$,

$$\frac{\lambda_o}{\omega^2} e^{\lambda_o(\frac{u-3}{4}(2H)-1)} C_{v-2} - \frac{\lambda_o}{\omega^2} e^{-\lambda_o(\frac{u-3}{4}(2H)-1)} C_{v-1} - \frac{\lambda_i}{\frac{1}{T}(kM-\omega^2)} e^{\lambda_i(\frac{u-3}{4}(2H)-1)} C_v + \frac{\lambda_i}{\frac{1}{T}(kM-\omega^2)} e^{-\lambda_i(\frac{u-3}{4}(2H)-1)} C_{v+1} = 0 \tag{D 3}$$

for odd u and odd $\frac{u-1}{2}$,

$$e^{\lambda_i(\frac{u-4}{4}(2H)+1)} C_{v-1} + e^{-\lambda_i(\frac{u-4}{4}(2H)+1)} C_v - e^{\lambda_0(\frac{u-4}{4}(2H)+1)} C_{v+1} - e^{-\lambda_0(\frac{u-4}{4}(2H)+1)} C_{v+2} = 0 \tag{D 4}$$

for even u and even $\frac{u}{2}$,

$$-\frac{\lambda_i}{\frac{1}{T}(kM-\omega^2)} e^{\lambda_i(\frac{u-5}{4}(2H)+1)} C_{v-2} + \frac{\lambda_i}{\frac{1}{T}(kM-\omega^2)} e^{-\lambda_i(\frac{u-5}{4}(2H)+1)} C_{v-1} + \frac{\lambda_o}{\omega^2} e^{\lambda_o(\frac{u-5}{4}(2H)+1)} C_v - \frac{\lambda_o}{\omega^2} e^{-\lambda_o(\frac{u-5}{4}(2H)+1)} C_{v+1} = 0 \tag{D 5}$$

for odd u and even $\frac{u-1}{2}$,

$$C_{2n+1} = 0, \tag{D 6}$$

for $u = 2n + 2$. The $\mp$ term in D 1 refers to a symmetric or anti-symmetric solution respectively. Equations D 2 and D 4 describe continuity of displacement whilst D 3 and D 5 describe continuity of pressure. In D 2 and D 3 the equations describe moving from a region outside of the jets to a region inside a jet, whilst D 4 and D 5 describing moving from within a jet to outside of it. Factors involving u and $2H$ in each of the exponential terms describe the location of the vortex sheet, along the y axis, where that boundary condition is applied. In this way 2.4 can then be built and subsequently solved to compute wavenumbers, k, for an n-planar jet system. For odd values of n the midpoint of the system lies through the middle of a jet (figure 20(b)). This changes the locations of both the symmetry line and vortex sheets forming a new set of equations,

$$C_1 \mp C_2 = 0, \tag{D 7}$$

for $u = 1$,

$$e^{\lambda_o(\frac{u-2}{4}(2H)+1)}C_{v+1} + e^{-\lambda_o(\frac{u-2}{4}(2H)+1)}C_{v+2} - e^{-\lambda_i(\frac{u-2}{4}(2H)+1)}C_{v-1} - e^{-\lambda_i(\frac{u-2}{4}(2H)+1)}C_v = 0, \tag{D 8}$$

for even u and odd $\frac{u}{2}$,

$$\frac{\lambda_o}{\omega^2}e^{\lambda_o(\frac{u-3}{4}(2H)+1)}C_v - \frac{\lambda_o}{\omega^2}e^{-\lambda_o(\frac{u-3}{4}(2H)+1)}C_{v+1} - \frac{\lambda_i}{\frac{1}{T}(kM-\omega^2)}e^{\lambda_i(\frac{u-3}{4}(2H)+1)}C_{v-2} + \frac{\lambda_i}{\frac{1}{T}(kM-\omega^2)}e^{-\lambda_i(\frac{u-3}{4}(2H)+1)}C_{v-1} = 0 \tag{D 9}$$

for odd u and odd $\frac{u-1}{2}$,

$$e^{\lambda_i(\frac{u}{4}(2H)+1)}C_{v+1} + e^{-\lambda_i(\frac{u}{4}(2H)-1)}C_{v+2} - e^{\lambda_0(\frac{u}{4}(2H)+1)}C_{v-1} - e^{-\lambda_0(\frac{u}{4}(2H)-1)}C_v = 0 \tag{D 10}$$

for even u and even $\frac{u}{2}$,

$$-\frac{\lambda_i}{\frac{1}{T}(kM-\omega^2)}e^{\lambda_i(\frac{u-1}{4}(2H)-1)}C_v + \frac{\lambda_i}{\frac{1}{T}(kM-\omega^2)}e^{-\lambda_i(\frac{u-1}{4}(2H)-1)}C_{v+1} + \frac{\lambda_o}{\omega^2}e^{\lambda_o(\frac{u-1}{4}(2H)-1)}C_{v-2} - \frac{\lambda_o}{\omega^2}e^{-\lambda_o(\frac{u-1}{4}(2H)-1)}C_{v-1} = 0 \tag{D 11}$$

for odd u and even $\frac{u-1}{2}$,

$$C_{2n+1} = 0, \tag{D 12}$$

for $u = 2n + 2$.

REFERENCES

Bayliss, Alvin & Turkel, Eli 1992 Mappings and accuracy for chebyshev pseudo-spectral approximations. *Journal of Computational Physics* **101** (2), 349–359.

Bell, G, Cluts, J, Samimy, M, Soria, J & Edgington-Mitchell, D 2021 Intermittent modal coupling in screeching underexpanded circular twin jets. *Journal of Fluid Mechanics* **910**, A20.

Crow, S. C. & Champagne, F. H. 1971 Orderly structure in jet turbulence. *Journal of Fluid Mechanics* **48** (3), 547–591.

Du, Zihua 1993 Acoustic and Kelvin-Helmholtz Instability Waves of Twin Supersonic Jets. PhD thesis, Department of Mathematics, The Florida State University, Florida.

Edgington-Mitchell, Daniel 2019 Aeroacoustic resonance and self-excitation in screeching and impinging supersonic jets–a review. *International Journal of Aeroacoustics* **18** (2-3), 118–188.

Edgington-Mitchell, Daniel, Jaunet, Vincent, Jordan, Peter, Towne, Aaron, Soria, Julio & Honnery, Damon 2018 Upstream-travelling acoustic jet modes as a closure mechanism for screech. *Journal of Fluid Mechanics* **855**, R1.

Edgington-Mitchell, Daniel, Li, Xiangru, Liu, Nianhua, He, Feng, Wong, Tsz Yeung, Mackenzie, Jacob & Nogueira, Petronio 2022 A unifying theory of jet screech. *Journal of Fluid Mechanics* **945**, A8.

Edgington-Mitchell, Daniel, Wang, Tianye, Nogueira, Petronio, Schmidt, Oliver, Jaunet, Vincent, Duke, Daniel, Jordan, Peter & Towne, Aaron 2021 Waves in screeching jets. *Journal of Fluid Mechanics* **913**, A7.

Gojon, Romain, Bogey, Christophe & Mihaescu, Mihai 2018 Oscillation modes in screeching jets. *AIAA Journal* **56** (7), 2918–2924.

Harper-Bourne, M & Fisher, MJ 1974 The noise from shock waves in supersonic jets, noise mechanisms-agard conference on propagation and reduction of jet noise. *AGARD CP-131* pp. 11–1.

Jordan, Peter, Jaunet, Vincent, Towne, Aaron, Cavalieri, André VG, Colonius, Tim, Schmidt, Oliver & Agarwal, Anurag 2018 Jet–flap interaction tones. *Journal of Fluid Mechanics* **853**, 333–358.

Lessen, M, Fox, JA & Zien, HM 1965 The instability of inviscid jets and wakes in compressible fluid. *Journal of Fluid Mechanics* **21** (1), 129–143.

Mancinelli, Matteo, Jaunet, Vincent, Jordan, Peter & Towne, Aaron 2019 Screech-tone prediction using upstream-travelling jet modes. *Experiments in Fluids* **60** (1), 22.

Mancinelli, Matteo, Jaunet, Vincent, Jordan, Peter & Towne, Aaron 2021 A complex-valued resonance model for axisymmetric screech tones in supersonic jets. *Journal of Fluid Mechanics* **928**, A32.

Martini, Eduardo, Cavalieri, André V. G. & Jordan, Peter 2019 Acoustic modes in jet and wake stability. *Journal of Fluid Mechanics* **867**, 804–834.

Merle, Mlle Marie 1957 Nouvelles recherches sur les fréquences ultrasonores émises par les jets d'air. In *Annales des Télécommunications*, , vol. 12, pp. 424–426. Springer.

Michalke, Alfons 1970 A note on the spatial jet-instability of the compressible cylindrical vortex sheet. *Tech. Rep.*. Deutsche Forschungs-und Versuchsanstalt für Luft- und Raumfahrt. FB-70-51.

Michalke, Alfons 1971 Instabilitaet eines kompressiblen runden freistrahis unter berucksichtigung des einflusses der strahigrenzschichtdicke (instability of a compressible circular jet considering the influence of the thickness of the jet boundary layer). *Z. Flugwiss* **19**, 319–328. English translation: NASA TM 75190, 1977.

Mollo-Christensen, Erik 1967 Jet Noise and Shear Flow Instability Seen From an Experimenter's Viewpoint. *Journal of Applied Mechanics* **34** (1), 1–7.

Morris, Philip J 1990 Instability waves in twin supersonic jets. *Journal of Fluid Mechanics* **220**, 293–307.

Morris, Philip J 2010 The instability of high speed jets. *International Journal of Aeroacoustics* **9** (1-2), 1–50.

Nogueira, Petrônio AS & Edgington-Mitchell, Daniel M 2021 Investigation of supersonic twin-jet coupling using spatial linear stability analysis. *Journal of Fluid Mechanics* **918**, A38.

Nogueira, Petrônio AS, Jaunet, Vincent, Mancinelli, Matteo, Jordan, Peter & Edgington-Mitchell, Daniel 2022 Closure mechanism of the a1 and a2 modes in jet screech. *Journal of Fluid Mechanics* **936**, A10.

Powell, Alan 1953 On the mechanism of choked jet noise. *Proceedings of the Physical Society. Section B* **66** (12), 1039.

Powell, Alan, Umeda, Yoshikuni & Ishii, Ryuji 1992 Observations of the oscillation modes of choked circular jets. *The Journal of the Acoustical Society of America* **92** (5), 2823–2836.

Raman, Ganesh 1999 Supersonic jet screech: half-century from powell to the present. *Journal of Sound and Vibration* **225** (3), 543–571.

Raman, Ganesh, Panickar, Praveen & Chelliah, Kanthasamy 2012 Aeroacoustics of twin supersonic jets: a review. *International Journal of Aeroacoustics* **11** (7-8), 957–984.

Rodríguez, Daniel 2021 Wavepacket models for supersonic twin-jets. In *AIAA AVIATION 2021 FORUM*. AIAA Paper 2021-2121.

Rodríguez, Daniel, Jotkar, Mamta R & Gennaro, Elmer M 2018 Wavepacket models for subsonic twin jets using 3d parabolized stability equations. *Comptes Rendus Mécanique* **346** (10), 890–902.

Rodríguez, Daniel, Stavropoulos, Michael N, Nogueira, Petronio AS, Edgington-Mitchell, Daniel & Jordan, Peter 2022 On the preferred flapping motion of round twin jets. *Journal of Fluid Mechanics arXiv:2210.07665* **In review**.

Seiner, John M, Manning, James C & Ponton, Michael K 1988 Dynamic pressure loads associated with twin supersonic plume resonance. *AIAA Journal* **26** (8), 954–960.

Shen, Hao & Tam, Christopher KW 2002 Three-dimensional numerical simulation of the jet screech phenomenon. *AIAA journal* **40** (1), 33–41.

Stavropoulos, Michael, Mancinelli, Matteo, Jordan, Peter, Jaunet, Vincent, Edgington-Mitchell, Daniel M & Nogueira, Petrônio 2022 Analysis of axisymmetric screech tones in round twin-jets using linear stability theory. In *28th AIAA/CEAS Aeroacoustics 2022 Conference*. AIAA Paper 2022-3071.

Stavropoulos, Michael, Mancinelli, Matteo, Jordan, Peter, Jaunet, Vincent, Weightman, Joel, Edgington-Mitchell, Daniel & Nogueira, Petrônio 2023 The axisymmetric screech tones of round twin jets examined via linear stability theory. *Journal of Fluid Mechanics* **Accepted**.

Tam, Christopher KW & Hu, Fang Q 1989 On the three families of instability waves of high-speed jets. *Journal of Fluid Mechanics* **201**, 447–483.

Tam, Christopher KW & Tanna, HK 1982 Shock associated noise of supersonic jets from convergent-divergent nozzles. *Journal of Sound and Vibration* **81** (3), 337–358.

Tam, Christopher K. W. & Ahuja, K. K. 1990 Theoretical model of discrete tone generation by impinging jets. *Journal of Fluid Mechanics* **214**, 67–87.

Towne, Aaron, Cavalieri, André VG, Jordan, Peter, Colonius, Tim, Schmidt, Oliver, Jaunet, Vincent & Brès, Guillaume A 2017 Acoustic resonance in the potential core of subsonic jets. *Journal of Fluid Mechanics* **825**, 1113–1152.

Trefethen, Lloyd N 2000 *Spectral methods in MATLAB*. SIAM.

van der Velden, Ellert 2020 Cmasher: Scientific colormaps for making accessible, informative and 'cmashing' plots. *Journal of Open Source Software* **5** (46), 2004.

Wong, Tsz Y.M., Stavropoulos, Michael N., Beekman, Jayson R., Towne, Aaron, Nogueira, Petrônio A.S., Weightman, Joel & Edgington-Mitchell, Daniel 2023 Steady and unsteady coupling in twin weakly underexpanded round jets. *Journal of Fluid Mechanics* **964**, A2.